Near-field thermoacoustic imaging with transmission line pulsers

Murad Omar and Stephan Kellnberger

Institute for Biological and Medical Imaging (IBMI), Technische Universität München and HelmholtzZentrum München, Ingolstädter Landstr. 1, D-85764 Neuherberg, Germany

George Sergiadis

Aristotle University, University Campus, 54124 Thessaloniki, Greece

Daniel Razansky and Vasilis Ntziachristosa)

Institute for Biological and Medical Imaging (IBMI), Technische Universität München and HelmholtzZentrum München, Ingolstädter Landstr. 1, D-85764 Neuherberg, Germany

(Received 30 September 2011; revised 23 May 2012; accepted for publication 30 May 2012; published 29 June 2012)

Purpose: Near-field radiofrequency thermoacoustic (NRT) tomography has been recently introduced for imaging electromagnetic (EM) properties of tissues using ultrawideband, high-energy impulses, which induce thermoacoustic responses. Operation in the near-field allows for more effective energy coupling into tissue, compared to using radiating sources, which in turn enables the use of shorter excitation pulses and leads to higher image resolution. This work aimed at investigating transmission lines as a method to generate excitation pulses to improve the NRT resolution over previous implementations without compromising the energy coupled into tissue.

Methods: The authors implemented a number of custom-made transmission lines to overcome the challenges of the broadband nature of the impulse excitation required in NRT. The authors further constructed phantoms and investigated the performance of the lines in regard to the pulse duration, energy coupling and the resulting resolution, and image quality achieved. Finally, the authors employed mice in order to investigate the performance of the approach in tissue imaging.

Results: The authors found that the use of transmission lines resulted in the generation of RF impulses in the range of tens of nanoseconds and shorter. This performance resulted to resolution improvements over previous thermoacoustic imaging implementations, reaching 45 μ m resolution, while retaining several tens to hundreds of milli-Joules of energy per pulse. This performance further allowed the visualization and clear differentiation of different mouse structures such as the heart, lung, or spinal cord.

Conclusions: The use of transmission lines significantly improved the NRT performance leading to high thermoacoustic tomography imaging quality by coupling adequate amounts of energy within short times at a relatively low cost. © 2012 American Association of Physicists in Medicine. [http://dx.doi.org/10.1118/1.4729710]

Key words: thermoacoustic tomography, biological imaging, impulse generator, small animal imaging

I. INTRODUCTION

Thermoacoustic tomography (TAT) has been considered since the early 1980s¹ to image soft tissues for medical applications. The technique is based on the transient absorption of electromagnetic energy by tissue or other dielectric material, followed by a corresponding temperature increase. The transient temperature rise leads to thermoelastic expansion and generation of broadband acoustic radiation. An advantage of thermoacoustic imaging over microwave imaging is that the spatial resolution achieved does not relate to the wavelength of the electromagnetic energy employed, but rather to the width of the excitation pulse and the frequency bandwidth of the ultrasound transducer used.

The use of pulses with durations in the nanosecond range can lead to TAT resolutions that are limited by the ultrasonic diffraction and can theoretically reach down to a few tens of microns or better. This is a significant betterment compared to conventional thermoacoustic imaging, where carrierfrequency modulated pulses are used for excitation, yielding pulse widths which are in the range of $0.5-1.0~\mu s.^{2-4}$ The use of long duration pulses is implicit in TAT using radiating sources to allow for sufficient energy delivery into tissue. However, such pulse durations lead to spatial resolution in the order of 0.7-1.5 mm, defined by the distance covered by sound during the duration of the excitation pulse. In addition, the high costs associated with the ultrahigh power amplifiers, used for generation of modulated pulses, further limits the applicability of this approach.

Recently, the use of impulse-driven thermoacoustic imaging, ^{5,6} has been proposed, where shorter duration highenergy impulses are generated in the tens of nanoseconds range in order to induce thermoacoustic signals in the imaged object, located in close vicinity (near-field) of the impulse generator. Due to the use of shorter pulses, nearfield imaging can lead to improvements in the imaging resolution achieved. Impulse-based near-field radiofrequency thermoacoustic (NRT) could potentially further lead to significant reduction of costs, allowed by the lower cost and manufacturing simplicity of radiofrequency impulse generators.

The ability to reduce the duration of pulses while maintaining efficient energy coupling can lead to further gains in the resolution achieved by TAT. To this end, generation of high-energy ultrawideband impulses with accurately defined spectral and energy characteristics is challenging. In response, we developed and investigated herein the utility of energy-storing transmission-lines, which allows the control of pulse duration without compromising the energy of the pulse. By operating in the near-field this energy can be efficiently coupled to the tissue imaged. We find that this approach brings significant advantages in terms of imaging performance, while utilizing easily accessible sources. In the following, we introduce the pulse generation system developed, describe its operational characteristics, and subsequently we showcase the best NRT images yet to date.

II. THEORY AND METHODS

II.A. Thermoacoustic signal generation

The generation of the thermoacoustic signal is based upon the thermoacoustic effect whereby an acoustic signal is generated, typically at ultrasonic frequencies, due to thermoelastic expansion of tissue caused by absorption of an electromagnetic pulse. The measured signal is governed by the thermoacoustic wave equation, ^{1,7–10}

$$\nabla^2 p(\vec{r}, t) - \frac{1}{v_s^2} \frac{\partial^2 p(\vec{r}, t)}{\partial t^2} = -\frac{\beta}{\kappa v_s^2} \frac{\partial^2 T(\vec{r}, t)}{\partial t^2}, \tag{1}$$

where $p(\vec{r},t)$ denotes the pressure generated at position \vec{r} and time t, v_s is the speed of sound in the medium ($v_s \approx 1500$ m/s for soft tissues), $T(\vec{r},t)$ is temperature variation in space and time, κ is the isothermal compressibility (for water or soft tissues $\kappa \approx 5 \times 10^{-10}$ Pa⁻¹), and β is the thermal coefficient of volume expansion (e.g., $\beta \approx 4 \times 10^{-4}$ K⁻¹ for muscles).^{7,8,10} The temperature field generation is governed by the heat equation, which in the case of thermoacoustics takes the form^{8,9}

$$\frac{\partial T(\vec{r},t)}{\partial t} - \alpha \nabla^2 T(\vec{r},t) = \frac{P_{\text{loss},D}(\vec{r},t)}{C_V}.$$
 (2)

In Eq. (2), α is the thermal diffusivity ($\alpha = 1.4 \times 10^{-7}$ m²/s for water), C_V is specific heat capacity at constant volume, and $P_{\text{loss}, D}$ is the power dissipated in the tissue of interest. The latter depends upon the amplitude of electromagnetic field variations as well as the electric characteristics of the medium and according to the Poynting's theorem, is given as 11,12

$$P_{\text{loss},D}(\vec{r},t) = \sigma(\vec{r})|\vec{E}(\vec{r},t)|^{2} + \pi f \varepsilon_{0} \varepsilon_{r}''(\vec{r})|\vec{E}(\vec{r},t)|^{2} + \pi f \mu_{0} \mu_{r}''(\vec{r})|\vec{H}(\vec{r},t)|^{2}.$$
(3)

In Eq. (3), $\sigma(\vec{r})$ is the spatial distribution of the electric conductivity, ε_0 and μ_0 are the electric permittivity and the magnetic permeability in free space, $\varepsilon''(\vec{r})$ is the imaginary part of the relative permittivity which describes the losses that are due to electric dipole relaxations, $\mu''(\vec{r})$ is the imaginary

part of the relative magnetic permeability which describes the magnetic losses within the medium, whereas $\vec{E}(\vec{r},t)$ and $\vec{H}(\vec{r},t)$ are the electric and magnetic fields induced in the medium.

A further assumption is that the heat is confined in space. This is realistic for ultrafast excitation combined with the low values of the thermal diffusivity α in water and soft tissue, leading to temperature changes which are significantly faster with respect to time than space. Then Eq. (2) reduces to

$$\frac{\partial T(\vec{r},t)}{\partial t} = \frac{P_{\text{loss},D}}{C_V}.$$
 (4)

Substituting Eq. (4) to Eq. (1) one obtains

$$\nabla^2 p(\vec{r}, t) - \frac{1}{v_s^2} \frac{\partial^2 p(\vec{r}, t)}{\partial t^2} = -\frac{\beta}{\kappa C_V v_s^2} \frac{\partial P_{\text{loss}, D}(\vec{r}, t)}{\partial t}.$$
 (5)

Subsequently, assuming only electric losses in Eq. (3), i.e., in the case of using a coupling element that emphasizes the electric-field component of the wave, and since normally $\mu'' = 0$ in biological tissues, Eq. (3) reduces to

$$P_{\text{loss},D}(\vec{r},t) = \sigma(\vec{r})|\vec{E}(\vec{r},t)|^2 + \pi f \varepsilon_0 \varepsilon_r''(\vec{r})|\vec{E}(\vec{r},t)|^2.$$
 (6)

If the excitation field wavelength is larger than the imaged object, the field can be approximated as homogenous throughout the volume of interest; thus, Eq. (6) can be rewritten in the form

$$P_{\text{loss},D}(\vec{r},t) = (\sigma(\vec{r}) + \pi f \varepsilon_0 \varepsilon_r''(\vec{r})) |\vec{E}(t)|^2.$$
 (7)

This formulation separates time and space dependencies in a way that the spatial part now depends only upon the electric properties of the imaging domain, i.e., conductivity $\sigma(\vec{r})$ and dielectric relaxation $\varepsilon''(\vec{r})$. Thus, effectively,

$$P_{\text{loss},D}(\vec{r},t) = P_{\text{loss},D}(\vec{r}) \cdot P_{\text{loss},D}(t), \tag{8}$$

i.e., the temporal part depends only on the excitation pulse. Use of Eq. (8) greatly simplifies image reconstruction, since one can now decompose the effects of the pulse shape using deconvolution, after measuring the excitation signal. This can lead to more accurate images of the underlining electric properties of the medium. Tomographic reconstructions can subsequently be obtained by collecting the generated thermoacoustic responses from multiple angles (projections) around the imaged object, followed by the use of inverse algorithms in order to obtain distribution of the electric losses.

Equation (6) further shows that the electric losses are divided between conductivity losses and relaxation losses. Nonetheless, for frequencies below 100 MHz conductivity losses for biological materials dominate over relaxation losses. This could be observed by using a Debye model for biological tissue, ¹³

$$\hat{\varepsilon} = \varepsilon_{\infty} + \frac{\varepsilon_s - \varepsilon_{\infty}}{1 + i\omega\tau} + \frac{\sigma_i}{i\omega\varepsilon_0},\tag{9}$$

where $\hat{\epsilon}$ is a term that describes the total permittivity and its imaginary part describes the total electric loss due to conductivity and relaxation. The imaginary part in this case is written as

$$\Im\left\{\hat{\varepsilon}\right\} = \frac{\omega\tau\left(\varepsilon_s - \varepsilon_\infty\right)}{1 + (\omega\tau)^2} + \frac{\sigma_i}{\omega\varepsilon_0}.\tag{10}$$

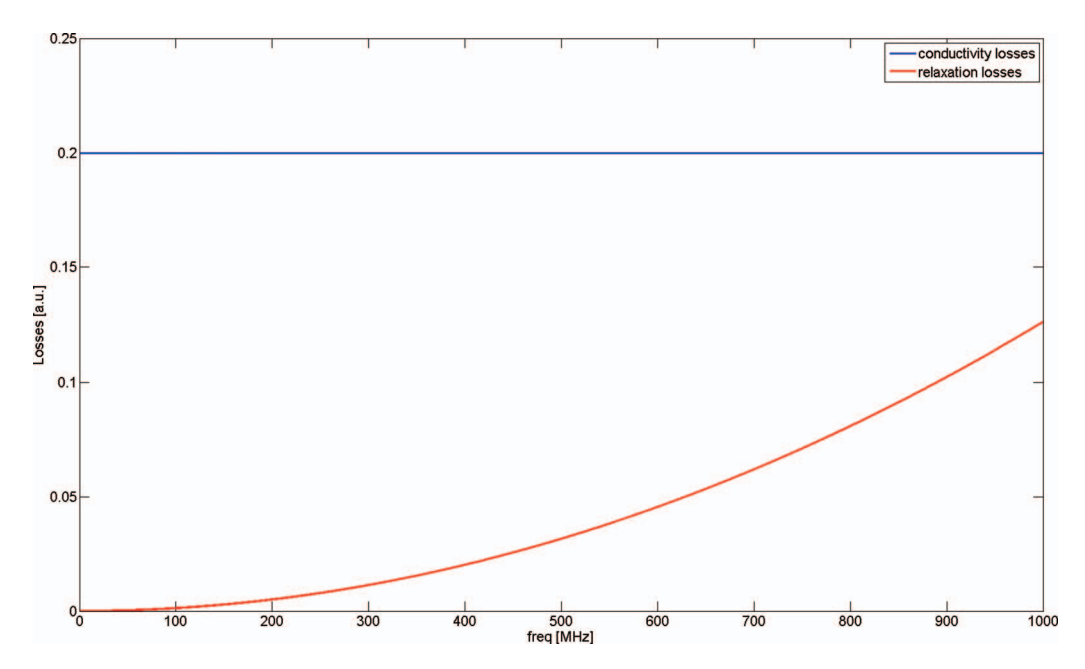


FIG. 1. Comparison between the electric losses due to conductivity (horizontal line) and the electric losses due to permittivity (increasing line). This clearly shows that within the frequency range <100 MHz the conductivity losses dominate.

oltage

source

By multiplying Eq. (10) by $\omega \varepsilon_0$ one obtains

$$\omega \varepsilon_0 \Im \left\{ \hat{\varepsilon} \right\} = \frac{\omega^2 \varepsilon_0 \tau \left(\varepsilon_s - \varepsilon_\infty \right)}{1 + \left(\omega \tau \right)^2} + \sigma_i. \tag{11}$$

To identify which part of Eq. (11) is dominant at different frequency ranges, it is useful to plot the first part of Eq. (11), which depends on the relaxation of electric dipoles, and the second part of Eq. (11), which depends on the conductivity versus frequency. Figure 1 shows such a plot for tissue parameters taken from Gabriel *et al.* for muscles.¹³

It is clear from Fig. 1 that for the frequency range below 100 MHz conductivity losses dominate over relaxation losses. The benefit of using low frequencies for tissue excitation is that the attenuation at lower frequencies is much lower than at higher frequencies, the penetration depth which is a term that describes the decay of electromagnetic waves inside a material is the depth at which the intensity or power of the field decays to 1/e of its surface value. For instance, the penetration depth in biological tissues with high water content such as skin and muscle is 91.3 cm at 1 MHz but drops to 21.6 cm at 10 MHz and 6.66 cm at 100 MHz and even lower at higher frequencies, ¹⁴ this corresponds to attenuations of 4.8 dB/m, 20.1 dB/m, and 65 dB/m, respectively.

II.B. Generation of high-power nanosecond pulses

Nanosecond pulses of high energy are essential for effective thermoacoustic signal generation. Such pulses can be produced by pulse compression, i.e., conversion of low power long duration pulses into high-power short duration output of equal energy. While short duration is necessary for obtaining high spatial resolution, the high excitation energy ensures generation of measurable thermoacoustic signal levels.

Recently, an impulse-driven thermoacoustic tomography method has been introduced that uses a high-voltage capacitor as the energy storage element,^{5,6} as shown in Fig. 2(a). This system was able to deliver ultrashort duration impulses of below 30 ns and has been subsequently used to create images from phantoms and small animals *ex vivo*.⁶ However, this pulser has a galvanic connection of the load to the high-voltage source and the coupling capacitor serves both as an energy reservoir and as a pulse shaping element.

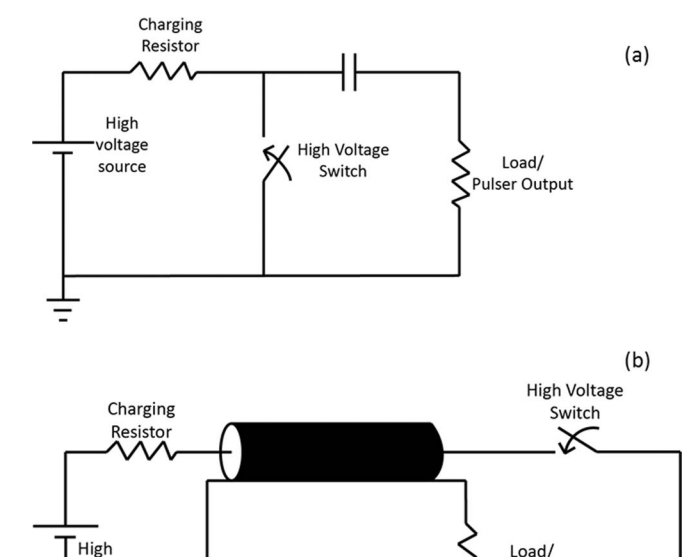


FIG. 2. Ultrashort duration impulse generation using a high-voltage capacitor (a) and transmission lines (b). In both cases the same switch and the same high-voltage source were used.

ulser Output

Herein, a new impulse generation approach was instead considered, which was based on storing the energy and forming the pulse within a distributed element topology, i.e., a transmission line, rather than a capacitor as shown in Fig. 2(b). For a transmission line pulser one can scale the pulse duration by changing the length of the transmission line according to 15

$$\tau_{\text{pulse}} = \frac{2\ell_{\text{line}}}{c},\tag{12}$$

whereby $c = c_0/\sqrt{\varepsilon_r}$ is the phase velocity of the wave over the line, $c_0 = 3 \times 10^8$ m/s is the phase velocity of electromagnetic waves in free space, and ε_r is the relative permittivity of the dielectric separating the outer and the inner conductors. The amount of the stored energy in the transmission line pulser is given by the following equation:

$$E_0 = \frac{1}{2}CV^2, (13)$$

whereby E_0 is the amount of the stored energy, C is the capacitance of the line, and V is the charging voltage, as seen the amount of the energy could be increased by either raising the charging voltage, or by adding more and more lines in parallel, the increase in the stored energy in this case is proportional to the number of the lines, i.e., $E_{\text{total}} = N_{\text{lines}} \times E_0$.

II.C. Experimental setup

The experimental setup of thermoacoustic tomographic imaging employed in the studies herein is depicted in Fig. 3 and utilized an impulse generator that was based on the homemade transmission line pulser. The pulser consisted of high-voltage coaxial lines (167-8556, Teledyne Reynolds), of three different lengths, i.e., 0.5 m, 1 m, and 2 m, having very low attenuation at frequencies of up to 400 MHz. The output of the pulser was connected to helically shaped energy coupling element, which was used to couple the electromagnetic energy to the imaged tissues. Even though such an energy coupling element has no directivity, a lossy object placed in its vicinity will regardless absorb a large part of the dissipated energy. A spark-gap capable of switching voltages of up to

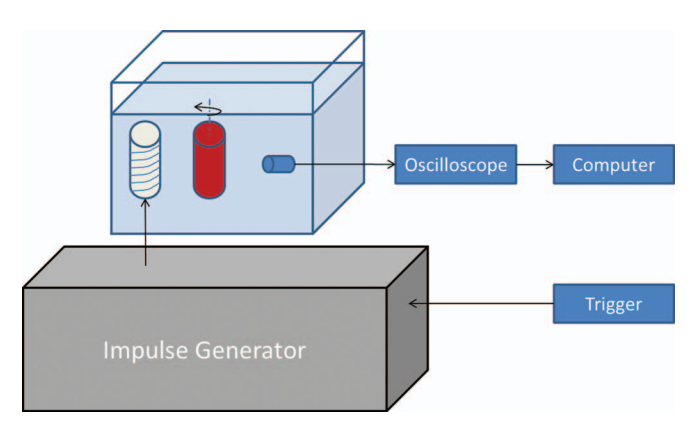


FIG. 3. Schematic diagram of the tomographic system, showing the major parts of the system, such as the pulser, the energy coupling element, and the acquisition.

36 kV within nanoseconds was used as a switch. The triggering of the spark-gap was done using a function generator (DG-1022, Rigol Technologies Inc.), which feeds the trigger circuitry with triggering pulses at 10 Hz repetition rate. To increase the delivered energy, three transmission lines were connected in parallel. A 30 kV high-voltage dc module (30C24-N125, HVProducts, USA) was used for charging the transmission lines. For tomographic measurements, imaged objects and animals were placed onto a rotation stage (PRM1Z8, Thorlabs Inc.), which rotated the imaged objects over 360°. The generated thermoacoustic signals were detected by a cylindrically focused ultrasonic transducer (Model V382, Panametrics, Olympus NDT, USA). The detected signals were subsequently fed into a low-noise amplifier with 63 dB gain (AU-1291, MITEQ Inc., USA), and sampled by a digital oscilloscope (TDS3054B, Tektronix Inc., USA). Synchronization and control of the hardware was done using MATLAB software (Mathworks Inc., Natick, MA). Image reconstruction was performed using the delay and sum algorithm, which is a special case of the filtered backprojection algorithm¹⁶ with statistical weighting.¹⁷

II.D. Reconstruction algorithm

For image reconstruction we employed a delay and sum algorithm^{10,18} with statistical weighting.¹⁷ The algorithm is a special case of the filtered back-projection algorithm and is based on an analytical solution to Eq. (5), i.e.,

$$p(\vec{r},t) = C \frac{\partial}{\partial t} \int_{S'} \frac{P_{\text{loss},D}(\vec{r}')}{|\vec{r} - \vec{r}'|} dS', \tag{14}$$

where S' is a time dependent spherical surface for which $|\vec{r} - \vec{r}'| = ct$. Equation (14) establishes that the pressure $p(\vec{r},t)$ in a homogeneous acoustic medium is solely due to the energy absorption at locations \vec{r}' so that the generated waves require time t to reach \vec{r} . For reconstructing the absorbed energy $P_{\text{loss},D}(\vec{r})$ there exists several approximate algorithms, such as the back-projection, 10,16 and the delay and sum algorithm, 10,16 which is a special case of the back-projection algorithm. For the general case

$$P_{\text{loss},D}(\vec{r}') \approx \int_{\Omega} \frac{d\Omega}{\Omega} \left[p(\vec{r},t) - t \frac{\partial p(\vec{r},t)}{\partial t} \right]_{t=|\vec{r}-\vec{r}'|/c}, \quad (15)$$

where $\Omega = 4\pi \cdot d\Omega$ is the solid angle for an element dS and acts as a weighting factor in the reconstruction. If the term $t \frac{\partial p}{\partial t}$ is discarded, then the algorithm is called the delay and sum algorithm. Discretizing Eq. (15) in 2D generates the following approximation for $P_{\text{loss},D}(\vec{r})$:

$$P_{\text{loss},D}(\vec{r}'_j) \approx \sum_i p(r_i, t_{ij}), \tag{16}$$

where \vec{r}_i is the position of the *i*th transducer, \vec{r}_j' is the position of the *j*th point of the reconstruction region of interest, and $t_{ij} = |\vec{r}_i - \vec{r}_j'|/c$. To improve upon the effects of acoustic scattering and reflections inside the sample, a statistical filtering was applied.¹⁷ For each point in the medium, the filtering process assigns decreasing importance to measurements as the distance between the point and the detector increases.

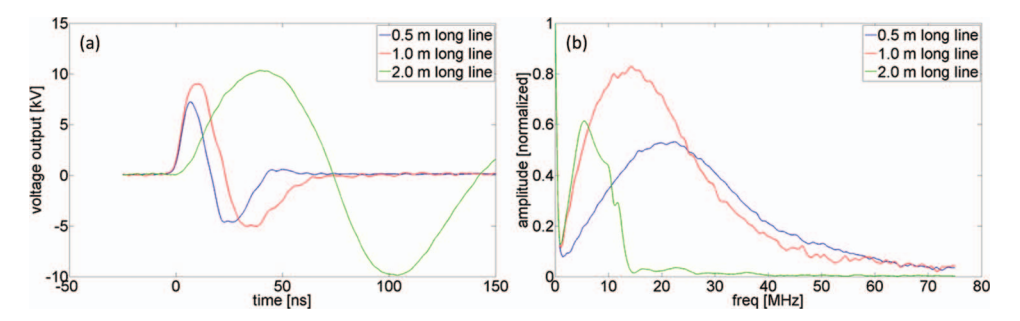


FIG. 4. Time domain (a) and frequency domain (b) comparison between the generated impulses using three different lengths of the transmission line.

The underlying rationale is that the further the point is from the detector the more probable it is that an acoustic reflection or an acoustic scattering event has happened.¹⁷

III. RESULTS

III.A. Pulser characterization

The three transmission lines of different lengths employed in the experimental setup were characterized for determining their operational specifications. Measurements of the pulse width and the amplitude were performed using a high-voltage probe (PHV 4002-3, PMK GmbH), connected to an oscilloscope (TDS3054B, Tektronix Inc., USA), this probe was connected to the output of the pulser.

The results are shown in Fig. 4. The 0.5 m line exhibited pulse duration of 10 ns, while 15 ns and 45 ns pulses were achieved by the 1 m and 2 m lines, respectively. Some deviations from ideal behavior can be attributed to the nonideal characteristics of the switch employed and nonperfect connections between the transmission line and the other components in the circuit. The generated impulse energies were 25 mJ, 49 mJ, and 260 mJ for the 0.5 m, 1 m, and 2 m lines, respectively, compared to 5–10 mJ/pulse used so far in conventional TAT setups. ^{18–20}

III.B. Phantom imaging

To assess the imaging performance achieved using transmission-line-based EM-pulses, phantoms of three PVC tubes of 3.5 mm diameter were employed. In one phantom shown in Fig. 5(a) three tubes filled with saline (0.9% NaCl) were imaged whereby in a second phantom, Fig. 5(b), two tubes filled with saline and a third tube filled with deionized water were imaged instead. Thermoacoustic measurements were performed using three 2 m long transmission lines connected in parallel, and the induced thermoacoustic signals were measured using a 3.5 MHz cylindrically focused transducer. The measurements were done in the tomographic setup of Fig. 3 using 180 projections over full rotation. At each projection, 16 averages were collected and images were reconstructed using the statistically weighted delay and sum method to suppress acoustic reflections. 17 Strong signals were recorded coming from the highly conductive saline and were clearly reconstructed as shown in Figs. 5(c) and 5(d). In comparison, the tube containing deionized water showed almost no contrast over the background.

Figure 5(e) depicts results from imaging a thin (50 μ m diameter) metallic wire immersed in deionized water. The wire was imaged using a 1m long transmission line, and the generated thermoacoustic signals were measured using a 15 MHz

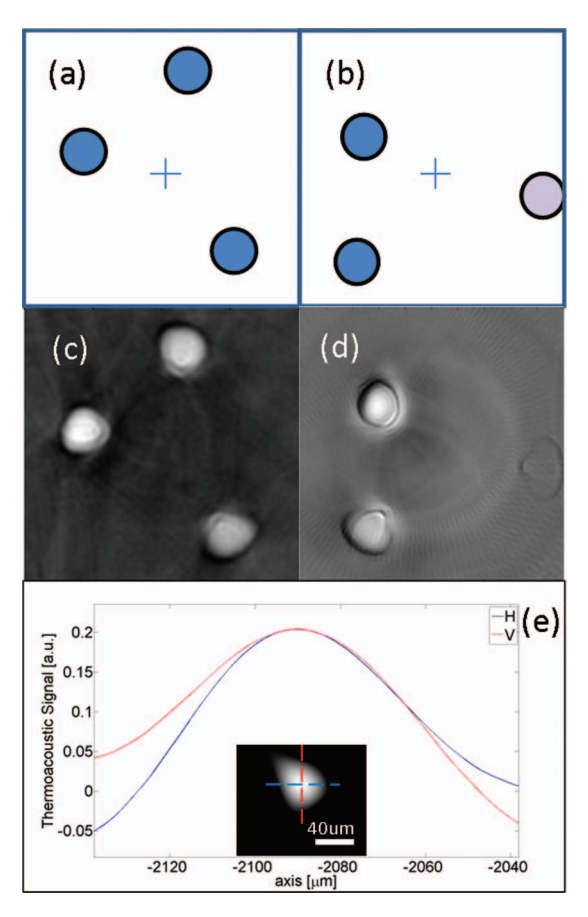


FIG. 5. Imaging performance characterization based on phantom studies (a) Schematic pf Phantom I made of three plastic tubes containing saline and immersed in deionized water. (b) Schematic of Phantom II consisting of three plastic tubes, two tubes containing saline and one containing deionized water, also immersed in deionized water. (c) Reconstruction image of Phantom I. (d) Reconstructed image of Phantom II. (e) Cross-sectional profiles from imaging a 50 μ m diameter metal wire. The inset shows a reconstruction of the wire using the filtered backprojection method. The line denoted by "H" shows a horizontal profile through the reconstruction (horizontal line in inset) whereby the line denoted by "V" shows a corresponding vertical profile through the reconstruction (vertical dotted line).

cylindrically focused transducer (Model V311, Panametrics, Olympus NDT, USA) using 180 projections over 360°. At each projection, 16 averages were collected. Since small objects emit mainly higher frequencies, image reconstruction was performed using the filtered backprojection algorithm with statistical weighting. ^{16,17}

Figure 5(e) shows a horizontal (H) and a vertical (V) profile through the reconstructed image of the wire shown in the inset. The achieved FWHM of the reconstructed profile is $\sim\!60~\mu\mathrm{m}$. Upon deconvolution from a 50 $\mu\mathrm{m}$ rectangular function, corresponding to the wire's profile, one obtains an estimate of the FWHM of the point spread function of the system to be $\sim\!45~\mu\mathrm{m}$, which is consistent with the resolution predicted by the upper part of the bandwidth measured by the ultrasonic transducer (the V311 records frequencies in the range of 2–22 MHz). This further implies that the use of the ultrashort pulses achieved herein enables thermoacoustic imaging resolution limited only by the acoustic diffraction.

III.C. Ex vivo mouse imaging

To examine the ability of the transmission line NRT system to imaging tissues, a full body scan of a CD1 adult mouse was performed. Prior to imaging, the mouse was shaved in order to improve acoustic coupling. For impulse generation, three transmission lines, 2 m long each, were connected in parallel. The acquired raw thermoacoustic data was then bandpassfiltered from 0.2 MHz to 4.0 MHz. Filtering generally increases the impulse response of the system (point-spread function) but it also helps to decrease the noise. The cut-off frequency of 4 MHz was selected so that a high-resolution image (100–200 $\mu \rm m$) of an entire mouse could be still produced, since large objects generate lower frequencies than, for example, in the case of the wire imaging in Fig. 5(e).

For reconstruction the delay and sum algorithm with statistical weighting was employed.¹⁷ In Fig. 6(a) 3D stack of reconstructed images obtained along the mouse is shown. Two representative slices from the thorax region are shown in Figs. 6(b) and 6(c) and are contrasted to corresponding pho-

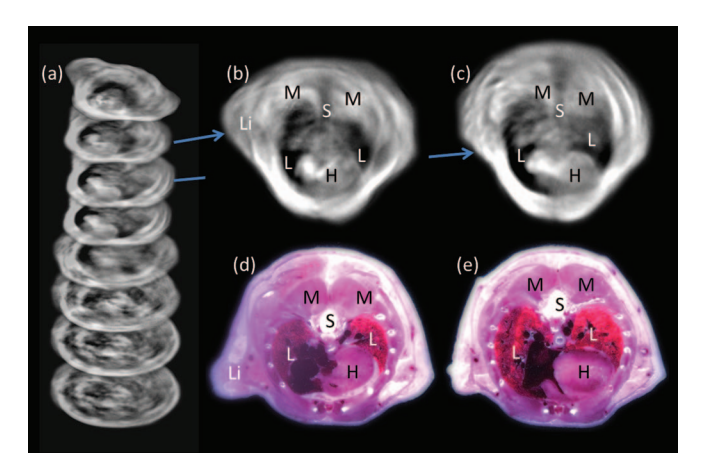


FIG. 6. Mouse measurements and corresponding cryoslices, TAI from different parts of the mouse (a) thermoacoustic slides showing several anatomical features [(b) and (c)] and corresponding cryoslices [(d) and (e)].

tographs obtained from cryoslices obtained at approximately the corresponding mouse location. The images clearly distinguish anatomical structures such as the heart (H) and tissues that surround the rib-cage revealing the lung (L). Other structures such as the spinal cord (S) and muscle tissue (M) are also visible and congruent with the same structures identified on the cryoslices.

IV. DISCUSSION

In this work, pulse generating transmission lines were introduced to implement high-resolution, NRT imaging. Compared to thermoacoustic tomography using radiating sources, NRT may improve the imaging resolution by more efficiently coupling energy in the near-field over far-field. This, in turn, enables the use of ultrashort duration impulses, in the nanosecond to tens of nanosecond range.

To achieve high-quality and energy excitation pulses, the use of transmission line pulse generators was considered herein and was found capable of producing ultrashort impulses while retaining high energy per pulse. Impedance matching of the transmission lines to the energy coupling element allowed for better energy transfer from the impulse generator to the energy coupling element, compared to previous spark-gap implementations. ^{5,6} In this way, electromagnetic energy in the range of 25–260 mJ could be coupled into the imaged tissue within ultrashort times, ranging from several nanoseconds to tens of nanoseconds.

The imaging performance of the system was examined on phantoms and animals. Compared to earlier NRT implementations, the images obtained appeared qualitatively better, offering significantly less artifacts and better organ and internal structure shape definition. Imaging resolution was found to be limited by the ultrasound detector characteristics, leading to a few tens of microns estimated resolution when employing a 15 MHz central-frequency ultrasonic detector. Importantly, the transmission lines employed make it possible to adjust flexibly the pulse duration to lead to even higher resolution when matched with appropriate acoustic detectors.

An additional feature of the method investigated is that the performance achieved relies on broadband radiofrequency excitation. Compared to narrowband implementations operating in the GHz range, 3,18–20 the use of broadband pulses allows potentially for deeper penetration and may lead in the future to practical portable implementations for clinical use. This hypothesis is corroborated by the fact that the excitation technology required in NRT is cost-effective and of small form factor. Future studies will involve the application of the method to *in vivo* investigation and the development of more efficient coupling elements to optimize the energy coupling to tissue. Future investigations should focus on examining the penetration depth vs resolution performance to better assess the clinical potential of the approach.

a) Author to whom correspondence should be addressed. Electronic mail: v.ntziachristos@tum.de; Telephone: +49 89 3187 3852; Fax: +49 89 3187 3017.

¹T. Bowen, "Radiation-induced thermoacoustic soft tissue imaging," Proc. IEEE Ultrason. Symp. **2**, 817–822 (1981).

- 4466
- ²R. A. Kruger, K. Stantz, and W. L. Kiser, Jr., "Thermoacoustic CT of the breast," in *Medical Imaging 2002: Physics of Medical Imaging* (SPIE, San Diego, 2002).
- ³R. A. Kruger, W. L. Kiser, Jr., D. R. Reinecke, G. A. Kruger, and R. L. Eisenhart, "Thermoacoustic computed tomography of the breast at 434 MHz," IEEE MTT-S Int. Microwave Symp. Dig. **2**, 591–594 (1999).
- ⁴M. Xu *et al.*, "Microwave-induced thermoacoustic tomography using multi-sector scanning," Med. Phys. 28(9), 1958–1963 (2001).
- ⁵D. Razansky, S. Kellnberger, and V. Ntziachristos, "Near-field radio-frequency thermoacoustic tomography with impulse excitation," Med. Phys. **37**(9), 4602–4607 (2010).
- ⁶S. Kellnberger, A. Hajiaboli, D. Razansky, and V. Ntziachristos, "Nearfield thermoacoustic tomography of small animals," Phys. Med. Biol. **56**, 3433–3444 (2011).
- ⁷V. Z. Gusev and A. A. Karabutov, *Laser Optoacoustics* (Springer, Berlin, 1993).
- ⁸R. A. Kruger and P. Liu, "Photoacoustic ultrasound: Pulse production and detection in 0.5% liposyn," Med. Phys. 21(7), 1179–1184 (1994).
- ⁹Y. Richard Fang, "Photoacoustic ultrasound (PAUS)-reconstruction tomography," Med. Phys. 22(10), 1605–1609 (1995).
- ¹⁰L. V. Wang and H.-I. Wu, Biomedical Optics: Principles and Imaging (Wiley Interscience, Hoboken, NJ, 2007).
- ¹¹D. Pozar, *Microwave Engineering*, 3rd ed. (Wiley, New York, 2005).

- ¹²C. A. Balanis, Advanced Engineering Electromagnetics (Wiley, New York, 1989).
- ¹³S. Gabriel, R. W. Lau, and C. Gabriel, "The dielectric properties of biological tissues: III. Parametric models for the dielectric spectrum of tissues," Phys. Med. Biol. 41, 2271–2293 (1996).
- ¹⁴C. Johnson and A. Guy, "Nonionizing electromagnetic wave effects in biological materials and systems," Proc. IEEE 60(6), 692–718 (1972).
- ¹⁵J. Mankowski and M. Kristiansen, "A review of short pulse generator technology," IEEE Trans. Plasma Sci. 28(1), 102–108 (2000).
- ¹⁶M. Xu and L. V. Wang, "Universal back-projection algorithm for photoacoustic computed tomography," Phys. Rev. E 71, 016706 (2005).
- ¹⁷X. Luis Dean-Ben, R. Ma, D. Razansky, and V. Ntziachristos, "Statistical approach for optoacoustic image reconstruction in the presence of strong acoustic heterogeneities," IEEE Trans. Med. Imag. 30(2), 401–408 (2011).
- ¹⁸G. Ku and L. V. Wang, "Scanning microwave-induced thermoacoustic tomography: Signal, resolution, and contrast," Med. Phys. 28(1), 4–10 (2000).
- ¹⁹L. V. Wang, X. Zhao, H. Sun, and G. Ku, "Microwave-induced acoustic imaging of biological tissues," Rev. Sci. Instrum. 70(9), 3744–3748 (1999).
- ²⁰R. A. Kruger, D. R. Reinecke, and G. A. Kruger, "Thermoacoustic computed tomography-technical considerations," Med. Phys. 26(9), 1832–1837 (1999)